www.acsnano.org

# Single-Step Dual-Layer Photolithography for Tunable and Scalable Nanopatterning

Wenfei Liu, Jiabao Wang, Xiuzhen Xu, Chuanzhen Zhao, Xiaobin Xu,\* and Paul S. Weiss\*



Downloaded via CZECH TECHL UNIV IN PRAGUE on October 28, 2024 at 16:25:42 (UTC). See https://pubs.acs.org/sharingguidelines for options on how to legitimately share published articles.

Cite This: ACS Nano 2021, 15, 12180-12188



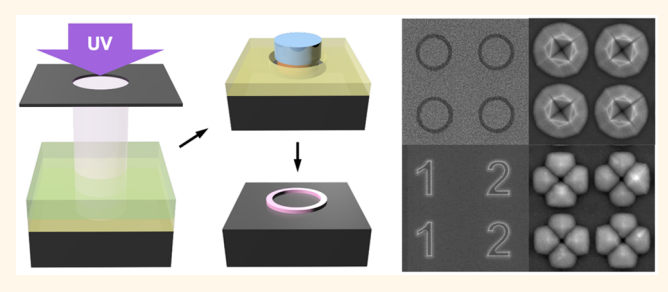
ACCESS

III Metrics & More

Article Recommendations

Supporting Information

ABSTRACT: Conventional photolithography, due to its scalability, robustness, and straightforward processes, has been widely applied to micro- and nanostructure manufacturing in electronics, optics, and biology. However, optical diffraction limits the ultimate resolution of conventional photolithography, which hinders its potential in nanoscale patterning for broader applications. Here, we introduce a derivative of conventional photolithography for nanoscale patterning called dual-layer photolithography (DLPL), which is based on the controlled exposure and development of overlapping positive and negative



photoresists. In a typical experiment, substrates are sequentially coated by two layers of photoresists (both positive and negative). Then, we purposefully control the exposure time to generate slightly larger features in the positive photoresist than those in the negative photoresist. After development, their overlapping areas become the final features, which outline the original features. We demonstrate line widths down to 300 nm here, which can be readily improved with more precise control. By adjusting the lithography parameters and material deposition, the feature sizes, shapes (e.g., rings, numbers, letters), line widths (300-900 nm), and materials (e.g., SiO<sub>2</sub>, Cr, and Ag) of these features can be independently controlled. Combined with anisotropic etching, more complex three-dimensional nanostructures can be fabricated as well, as we demonstrate here with Si. We further fabricate photodetectors as an example application to show that these nanostructures fabricated by DLPL can be used to promote light-trapping MAPbI<sub>3</sub> perovskite films to achieve good photoelectric properties. This strategy is not limited to ultraviolet photolithography and may also be incorporated into other energetic beam-based lithographic approaches, including deep and extreme ultraviolet photolithographies and electron beam lithography, to enhance their resolution.

KEYWORDS: photolithography, nanopatterning, nanofabrication, photodetector, nanoring

anolithography is a critical step in the fabrication processes of miniaturized electronic 1-5 and optical<sup>6–9</sup> devices. Conventional photolithography, using ultraviolet (UV) light to transfer features from photomasks to substrates, has been widely applied to micro- and nanoelectronics manufacturing due to its high throughput and high pattern fidelity. However, its feature resolution is limited by light diffraction and processing parameters. With recent advances in nanoscience and nanotechnology, nanometerscale resolution is increasingly needed for emerging applications. 10,111 For example, microfluidic chips with submicron structures have been developed for advanced biomedical applications (e.g., bioanalysis, cell regulation, drug delivery). 12-14 Additionally, submicron- and nanoscale structures can be integrated into optic and electric devices (e.g., optoelectronic circuits, displays, plasmonic sensors) for improved performance, sensitivity, and efficiency. 15-17

To overcome the resolution limit in conventional photolithography, advanced lithography techniques have been

developed with advanced light sources with smaller wavelengths, including deep UV (DUV) and extreme UV (EUV) photolithography, 18,19 electron-beam lithography (EBL), 20-22 and focused ion beam lithography (FIB). 23-25 Although these advanced techniques have been widely used in nanoelectronics, high equipment costs (DUV, EUV) or time-consuming serial writing processes (EBL, FIB) have greatly limited their availability and practicality for laboratories in universities, research institutions, and startups, 26 while the development of low-cost and high-throughput nanolithography approaches remains a challenge.

Received: May 1, 2021 Accepted: June 22, 2021 Published: June 25, 2021





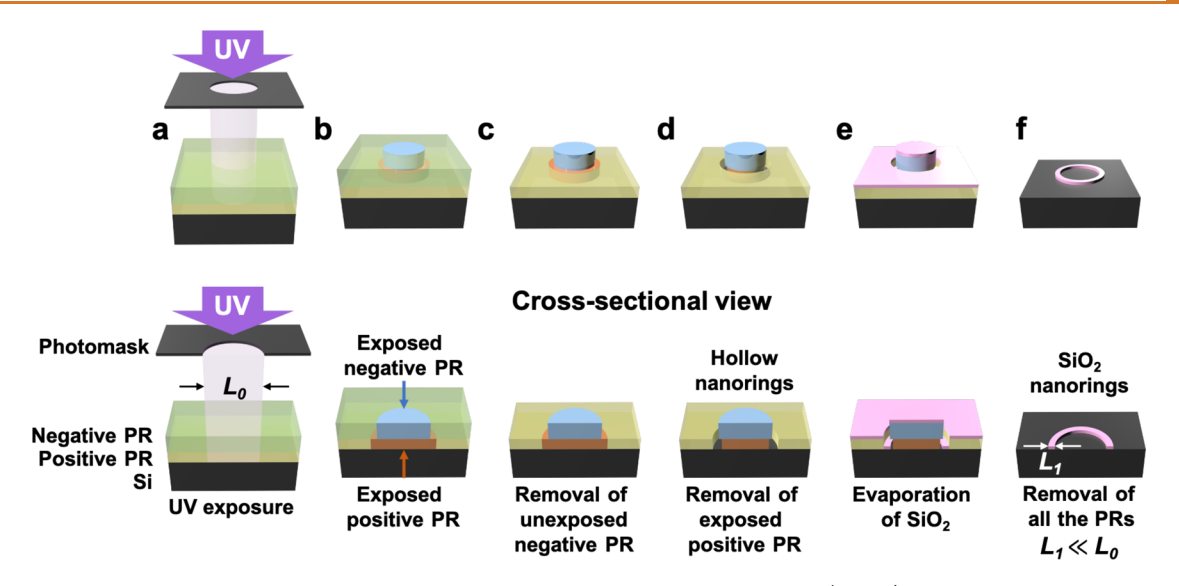


Figure 1. Fabrication schematics of SiO<sub>2</sub> nanorings by single-step dual-layer photolithography (DLPL). Top, overall process; bottom, cross-sectional view. (a) One-time UV exposure on dual-layer photoresists. (b) Postbaking after removing photomask. (c) First development of negative photoresist layer. (d) Second development of positive photoresist. (e) Deposition of SiO<sub>2</sub> thin film *via* magnetron sputtering. (f) Removal of dual-layer photoresists and generation of SiO<sub>2</sub> nanorings. PR: photoresist.

To address this challenge, various unconventional lithographic approaches and strategies have been developed, such as nanoimprint lithography, 27–29 soft lithography, 30–32 nanosphere lithography, 33,34 molecular ruler lithography, 35 and edge spreading lithography. For example, large-area metal nanoring arrays can be fabricated *via* a strategy that combines colloidal lithography and nanoscale electrodeposition. Moreover, by using the monolayers of self-assembled polymeric nanospheres as templates, multiple-patterning nanosphere lithography can be used to fabricate wafer-scale periodic hierarchical nanostructures. Although these lithographic methods reach high resolution with relatively low cost, the pattern quality and fidelity are strongly affected by the quality of the self-assembled templates and/or the quality of the stamps.

Meanwhile, efforts also have been made to push the resolution of conventional photolithography down to the nanometer scale through the optimization of the lithography parameters and processes. For example, immersion photolithography, 40 double-patterning photolithography, 41,42 and beam-pen lithography<sup>43</sup> have been developed to "overcome" the resolution limit. Specifically, double-patterning lithography can generate patterns with sizes several times smaller than the original features in photomasks through a subtraction process between two sequential patterns. However, its reproducibility relies on the alignment between the photomask and the patterns produced by each photolithographic step. Such processes require high-cost equipment for mask alignment. As a result, double patterning photolithography is limited due to the trade-off between increasing yield and decreasing alignment error.

In this work, we describe and demonstrate an alternative method to double-patterning photolithography, namely, dual-layer photolithography (DLPL). Without a mask alignment process or using high-refractive-index media, we realized tunable submicron patterning at high throughput and low cost. It is based on the controlled exposure and development of overlapping positive and negative photoresists to create hollow "outline-like" patterns. Note that, instead of creating undercuts

to facilitate the lift-off process as in other reported bilayer resist strategies, 44–47 DLPL is used here to scale down the feature size. The size, line width, material, and shape of the features can all be independently controlled in DLPL. Combined with anisotropic etching of Si, complex three-dimensional (3D) structures can and have been produced. We demonstrate the fabrication of photodetectors as an example application to show that nanostructures fabricated by DLPL can be used to promote light trapping in MAPbI<sub>3</sub> perovskite films to achieve good photoconductive properties. S0–52

# **RESULTS AND DISCUSSION**

A typical process of dual-layer photolithography for fabricating SiO<sub>2</sub> nanorings is illustrated in Figure 1. First, one layer of positive photoresist (in yellow) and one layer of negative photoresist (in green) were sequentially spin-coated with controlled thicknesses and soft-baked on piranha-cleaned Si substrates (piranha solution is a mixture of 3:1 sulfuric acid and 30% hydrogen peroxide. Warning: piranha solution reacts strongly with organic compounds and should be handled with caution; do not store in closed containers). A single controlled UV exposure was applied using a photomask patterned with 5  $\mu$ m hole arrays (Figure 1a). With the same amount of UV exposure, photoresponsivity variation resulted in slightly larger features on the positive photoresist than on the negative photoresist (Figure 1b). After removing the unexposed negative photoresist, circle-shaped features (in blue) were patterned on top of the positive photoresist layer (Figure 1c). The remaining negative photoresist hampered the complete removal of exposed positive photoresist (in orange) underneath, resulting in a dual-layer structure surrounded by hollow nanorings (Figure 1d). Next, a thin film of  $SiO_2$  (~30 nm) was deposited on the substrate via magnetron sputtering, resulting in the exposed Si nanoring arrays covered by SiO<sub>2</sub> film (Figure 1e). As the remaining SiO<sub>2</sub> thin film on top was lifted off with the photoresist removal, SiO<sub>2</sub> nanoring arrays were fabricated on Si substrates (Figure 1f).

To obtain the necessary photolithography parameters suitable for DLPL, which were not listed in the datasheet,

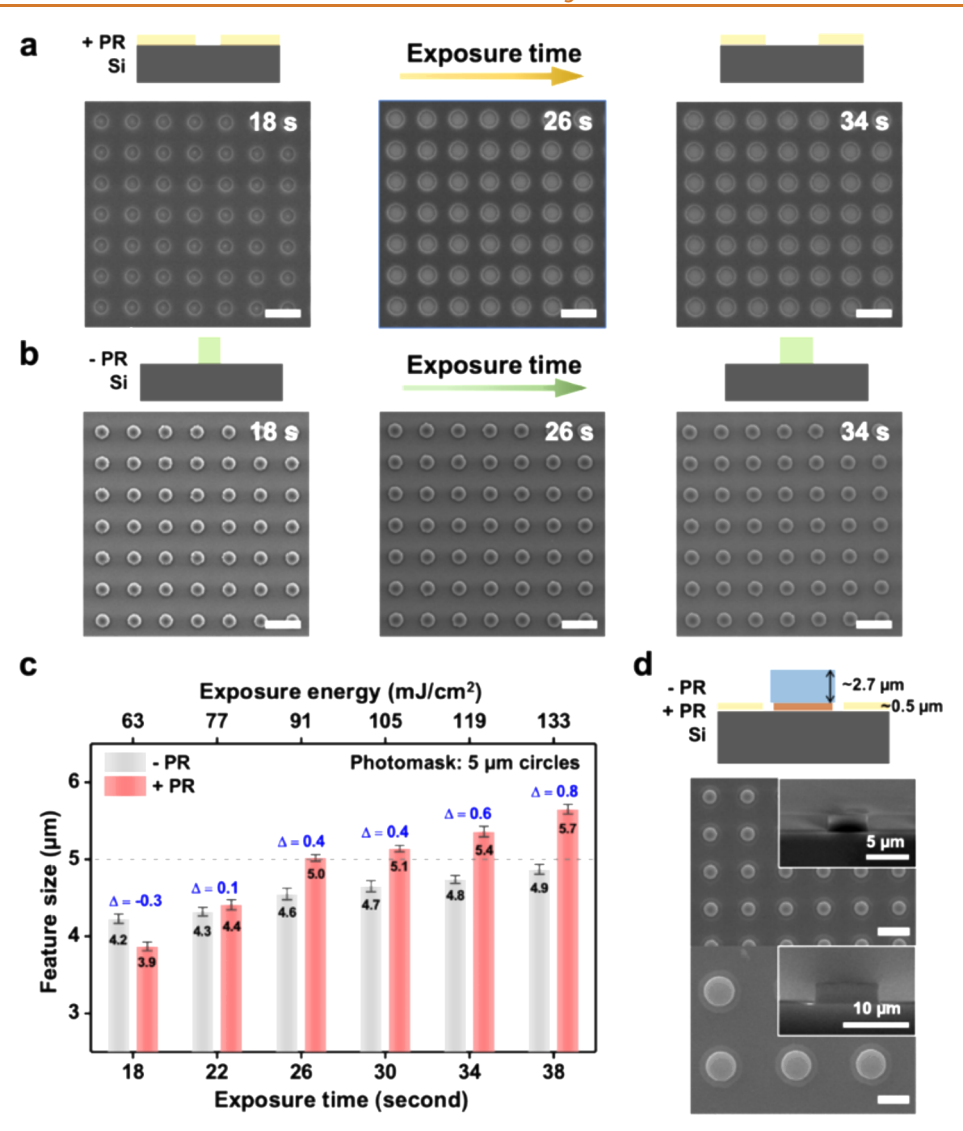


Figure 2. Systematic study of the pattern size dependence on the exposure time (or exposure energy) in dual-layer photolithography (DLPL). Scanning electron microscopy (SEM) images of single-layer photolithography for (a) positive photoresist and (b) negative photoresist with exposure times of 18, 26, and 34 s. Scale bar:  $5 \mu m$ . (c) Histogram of the size changes of features on positive and negative photoresists in the single-layer photolithography (SLPL) as the exposure time or corresponding exposure energy increased. (d) SEM top and side view images of the dual-layer structure after the development in DLPL with 30 s of exposure and the photomask feature sizes of 5 and 10  $\mu m$ . Scale bar: 10  $\mu m$ . PR: photoresist.

we studied the relationship between exposure time (t) and feature size (d) of each photoresist via designed single-layer photolithography (SLPL) using a Cr photomask with 5  $\mu$ m hole arrays. While exposure time was varied, other experimental parameters (e.g., UV light intensity, soft-baking time, development time) were held fixed. Theoretically, the feature sizes should increase with the added exposure time or exposure energy.<sup>53</sup> As a result, features generated by both photoresists shared similar size-increasing patterns (see Figure 2a,b). Overall, as the exposure time increased from 18 to 38 s, the feature size of the positive photoresist increased by 1.8  $\mu$ m  $(3.9-5.7 \mu m)$ , whereas the feature size of the negative photoresist increased by 0.7  $\mu$ m (4.2-4.9  $\mu$ m) (detailed measurements are provided in Table S1 of the Supporting Information). The higher feature size increase rate indicated a higher photoresponsivity of the positive photoresist than that of the negative photoresist.

To understand the dynamic changes in feature size, a series of SLPL experiments were conducted in parallel with the

exposure times set at 18, 22, 26, 30, 34, and 38 s (see Figure 2c; note the corresponding exposure energies shown). Note that for each condition, more than 10 samples were prepared and measured, which showed good reproducibility in feature sizes. The feature sizes of both photoresists with the same amount of exposure  $(d_{+PR})$  and  $d_{-PR}$  were provided in pairs. The size differences  $(\Delta = d_{+PR} - d_{-PR})$  were calculated to estimate the theoretical width (w) of hollow nanorings generated by DLPL under the same conditions. With 18 s of exposure, the features on the positive photoresist were smaller than those on the negative photoresist ( $\Delta = -0.3 \mu m$ ). Due to the higher responsivity of the positive photoresist, the size difference narrowed as the applied exposure time or exposure energy increased. At ~21 s, the feature sizes of both photoresists were equal. At longer times (>21 s), the features on the positive photoresist became larger than those on the negative photoresist ( $\Delta > 0 \mu m$ ). We thus predicted that a flip of the size difference would result in the formation of hollow nanorings in DLPL and that the theoretical ring width would

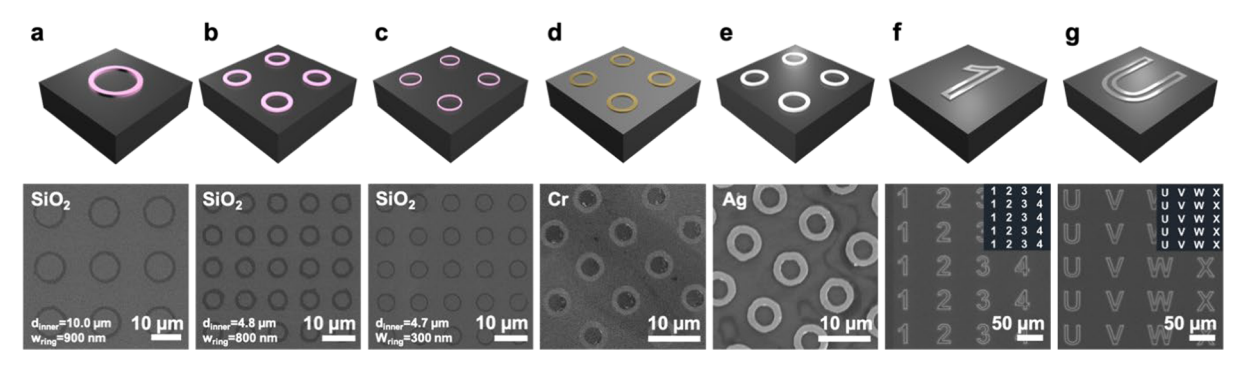


Figure 3. Scanning electron microscopy images of the nanopatterns fabricated by dual-layer photolithography with independent control of pattern parameters (i.e., size, line width, material, and shape): (a)  $SiO_2$  nanorings with inner diameter of 10  $\mu$ m and width of 900 nm; (b)  $SiO_2$  nanorings with inner diameter of 4.8  $\mu$ m and width of 800 nm; (c)  $SiO_2$  nanorings with inner diameter of 4.7  $\mu$ m and width of 300 nm; (d) Cr nanorings; (e) Ag nanorings; (f) metal patterns in number-shaped outlines with a line width of ~10  $\mu$ m; (g) metal patterns in letter-shaped outlines with a line width of ~10  $\mu$ m. Original AutoCAD photomask designs of number and letter patterns are provided in (f) and (g).

increase with increasing time (t = 21-26 s). However, this increase stopped as the exposure time rose from 26 to 30 s, and the size difference remained relatively constant ( $\Delta = 0.4 \mu m$ ). Within this range, the minimal size change ( $\sim 0.1 \mu m$ ) of both features made the size independent of the exposure time; varying the exposure time only resulted in subtle changes in the size difference. As the exposure time was increased further (t > 30 s), the size difference increased and reached 0.8  $\mu m$  (t = 38 s), which indicated that both photoresists experienced overexposure within the time range 30-38 s.

On the basis of the results of SLPL experiments, an optimal exposure time for DLPL was determined. In DLPL, since energy loss takes place when UV light penetrates the overlying negative photoresist, 53 the exposure energy received by the positive photoresist underneath is smaller compared to that of SLPL. As a result, the features generated by a positive photoresist in DLPL are equivalent to those generated with lower intensities or shorter exposure times in SLPL. Therefore, the widths of hollow nanorings obtained from DLPL are smaller than the corresponding estimates from SLPL. Although 22 s exposures produced the smallest size differences ( $\Delta = 0.1$  $\mu$ m) in SLPL, hollow nanorings with widths of 0.1  $\mu$ m were less likely to be realized in DLPL. According to the measured histogram (Figure 2c), both features demonstrated size uniformity as the exposure time increased from 26 to 30 s. Therefore, to minimize the size variations between SLPL and DLPL, a 30 s exposure was applied to the following DLPL

After development, the remaining photoresists formed a dual-layer 3D "cake" structure (Figure 2d). The negative photoresist layer had a thickness of ~2.7  $\mu$ m, whereas the positive photoresist layer had a thickness of ~0.5  $\mu$ m. As shown in Figure 2d, dual-layer structures in different sizes (5 and 10  $\mu$ m) were generated using the photomasks with the corresponding feature sizes. In the top view images, the central circles corresponded to the negative photoresist, while the outer rings corresponded to the hollow nanorings. The removal of the dual-layer structure was confirmed by the topographic differences shown in the side view images. The bright spots at each side of the "cake" structure were lower than the positive photoresist layer, which indicated that the Si surface was exposed.

We tested the versatility of DLPL by modifying the photolithography parameters and the material deposition **processes.** The graphic changes were visualized by depositing  $SiO_2$  or metals into the hollow "outline-like" patterns (*e.g.*, nanorings). Since the size of the hollow features depends strongly on the original features on the photomask, different feature sizes (*i.e.*, 10 and 5  $\mu$ m) could be realized using different photomasks (Figure 3a,b). In addition to feature size, the line widths of the hollow patterns could be independently controlled. On the basis of the results from SLPL, the theoretical width was proportional to the exposure time in the overexposure region ( $t \ge 30$  s). As a result,  $SiO_2$  nanorings with different widths (*i.e.*, 300 and 800 nm) were fabricated with different exposure times (*i.e.*, 30 and 38 s, respectively) (Figure 3b,c).

Furthermore, combined with material deposition, DLPL was used to fabricate nanostructures of different materials. Besides SiO<sub>2</sub> nanorings, Cr nanorings were fabricated *via* thermal evaporation (Figure 3d). Ag nanorings were fabricated similarly with predeposited Cr film (~5 nm) as an adhesive layer (Figure 3e). As shown, the nanorings fabricated with different materials were consistent in shape and size, which could be further applied as etching masks for reactive ion etching <sup>54,55</sup> and metal-assisted chemical etching. Notably, the widths of both Cr and Ag nanorings appeared larger than those of SiO<sub>2</sub> nanorings. We attribute these differences to the effects of diffusion in the thermal evaporation of metals, as compared to the magnetron sputtering of SiO<sub>2</sub>.

To reduce the effects of diffusion, we changed the order of deposition to fabricated hollow nanorings via a modified DLPL procedure. In this modified fabrication scheme, a Cr film (~30 nm) was thermally deposited on the Si substrate before photoresists were coated. After the development processes, the exposed Cr surface inside the hollow nanorings was wet-etched (etchant: 15 wt % diammonium cerium(IV) nitrate and 10 wt % hydrochloric acid in deionized water). After the removal of the photoresists, hollow nanorings were patterned on the Cr layer (Figure S1). The ring width was independently controlled by adjusting the etching time. This modified procedure provided a strategy to pattern hollow features on the surface of other materials besides Si, which could be further explored to assist in the further fabrication of complex structures.

Not limited to nanorings, the shapes of hollow features generated by DLPL were also tunable by using photomasks patterned with various features. To demonstrate the versatility

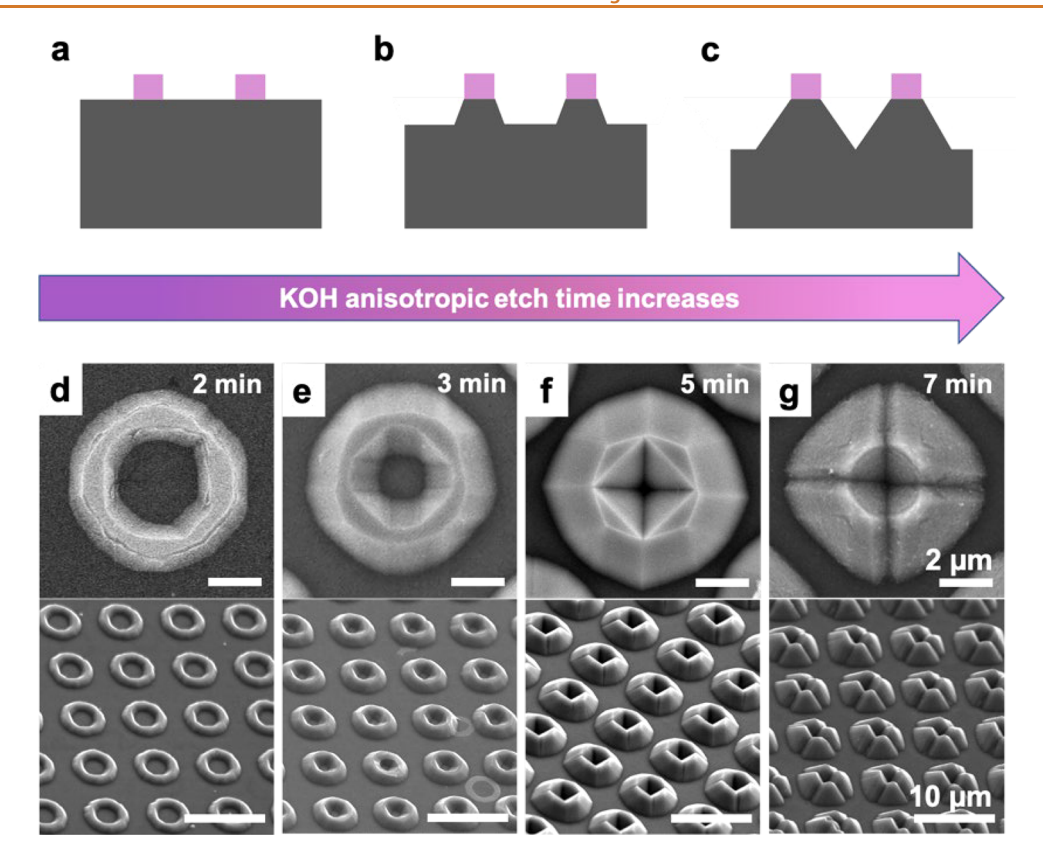


Figure 4. (a–c) Time-driven KOH anisotropic etching process of Si(100) substrates with a dual-layer-photolithography-fabricated  $SiO_2$  nanoring as the etching mask. Scanning electron microscopy images of morphologic transition of Si complex 3D nanostructures with etching times of (d) 2, (e) 3, (f) 5, and (g) 7 min. Top view of a single Si complex 3D nanostructure, and 45° tilt view of complex 3D nanostructure arrays.

of feature styles, photomasks patterned with numbers and letters with line widths of ~10  $\mu$ m were used. As a result, submicrometer metal patterns in the shapes of numbers and letter outlines were fabricated with line widths of ~1  $\mu$ m (Figure 3f,g). This scaling down (1:10) of various features demonstrated the effectiveness of DLPL in improving feature resolution with good pattern fidelity. Combined with the results shown above, we have achieved independent control of the feature size, line width, material, and shape in DLPL, indicating the adaptability and versatility of this nanopatterning method.

After 5  $\mu$ m SiO<sub>2</sub> nanorings were fabricated via DLPL, we demonstrated its application potential as an etching mask to assist Si nanofabrication. Since SiO<sub>2</sub> is etched much more slowly than Si under specific etching conditions (30 wt % KOH, 70 °C), the functionality of SiO<sub>2</sub> nanorings was investigated via KOH anisotropic etching of Si(100) substrates (Figure 4). As illustrated in Figure 4a, the etching process started on the surface of Si(100), which is also the  $\{100\}$  plane, and the {111} planes were revealed on the edge of the area protected by the SiO<sub>2</sub> nanoring (in violet). The lower atomic lattice density and more dangling bonds of {100} planes compared to {111} planes led to higher etching rates along the [100] direction in Si(100).<sup>58</sup> Subsequently, the {100} plane was etched down faster than the {111} plane as the etching time increased (Figure 4b). Once the anisotropic etching reached completion, the {100} plane became a point where the four {111} planes intersected (Figure 4c), resulting in an inverted pyramid inscribed in the SiO<sub>2</sub> nanoring.<sup>55</sup>

When the substrate was immersed into the KOH etching solution, the etching processes took place both inside and outside the SiO<sub>2</sub> nanoring. Although the {100} plane was the primary etching plane, other planes were also etched in the anisotropic etching process. As a result, the morphology of fabricated 3D nanostructures had a dynamic transition as the etching time increased. As shown in the SEM images, this time-driven transition was analyzed in four stages with etching durations of 2, 3, 5, and 7 min (Figure 4d-g)

At stage one (t=2 min), since the etching rate varied on each plane, the shape of the inside mask window changed from circles to octagons. Meanwhile, the outside mask windows maintained the circle shape (Figure 4d). The planes with higher etching rates were removed, while the remaining planes defined the boundary of the mask window. The Si $\{100\}$  planes were etched down to generate 3D nanostructures, resulting in isolated spaces inside the SiO<sub>2</sub> nanorings.

At stage two (t = 3 min), four sides on the octagon mask window were reduced while the other four were extended (Figure 4e). The decreased size of the  $\{100\}$  planes effectively resulted in the growth of the 3D nanostructure and the increased sizes of the exposed  $\{111\}$  planes. After removing the SiO<sub>2</sub> nanoring, the protected Si was smaller in width that at the previous stage, which indicated the growth of the undercut regions as the  $\{111\}$  planes were further etched.

At stage three (t = 5 min), as the four shorter sides of the octagon mask disappeared, the longer sides formed a square-shaped mask. Since the inside Si $\{100\}$  plane was etched down to a point, the  $\{111\}$  planes became the principal etching planes. Inverted pyramids were formed with measured sizes of

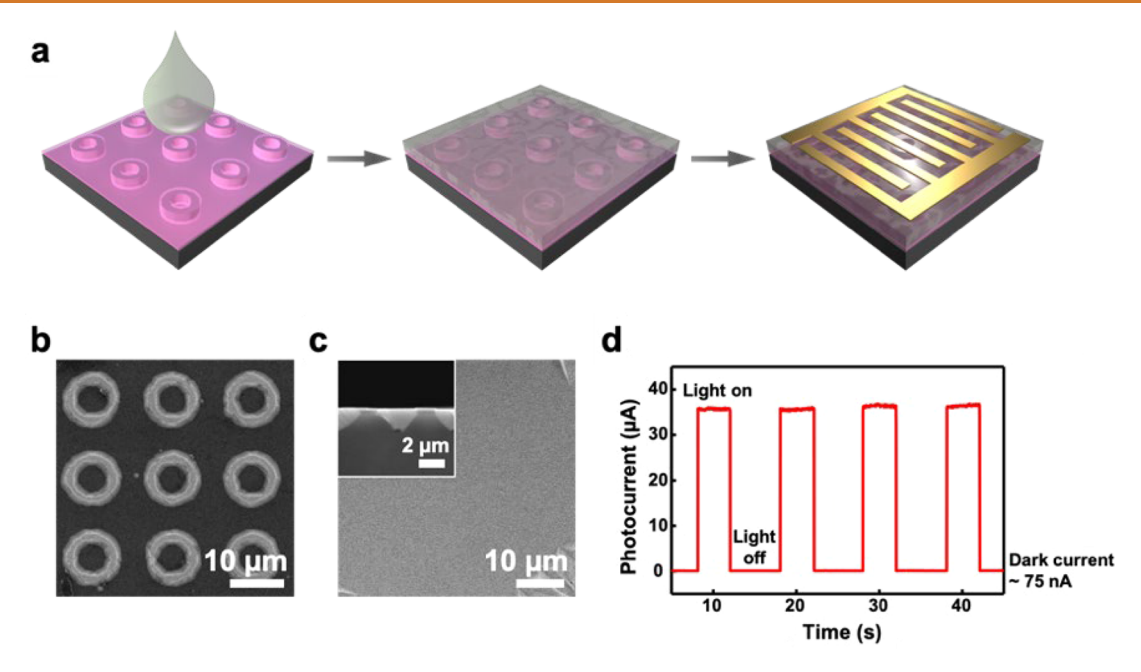


Figure 5. (a) Schematics of the MAPbI<sub>3</sub> film coating and interdigital electrode fabrication processes for the 2 min KOH-etched Si/SiO<sub>2</sub> 3D complex nanostructures. (b) Scanning electron microscopy (SEM) image of the 2 min KOH-etched Si complex 3D nanostructures coated with SiO<sub>2</sub> for isolation. (c) Top view and side view SEM images of the MAPbI<sub>3</sub> film coated on the Si/SiO<sub>2</sub> substrate. (d) Time-resolved light response curve of MAPbI<sub>3</sub>-based photodetector on the 2 min KOH-etched Si/SiO<sub>2</sub> nanostructure under a Xe lamp (10 mW/cm<sup>2</sup>).

 $\sim$ 3  $\mu$ m (Figure 4f). The presence of the undercut indicated that the inverted pyramid circumscribed the initial circle shape inside the mask window. After removing the SiO<sub>2</sub> nanoring, a connection at each corner of the inverted pyramid was observed. From the 45° tilt view, the inverted pyramid had a specific loading capacity isolated from the outside space due to the mask window defined (Figure S2). While anisotropic etching inside the SiO<sub>2</sub> nanoring reached completion, the outside etching process continued due to a larger {100} plane. As the {111} planes grew larger on the outside sidewall, the outside mask window started to transit from a polygon to an octagon. Notably, the diagonals of the mask windows on both sides were perfectly aligned. Therefore, we anticipated that, with further etching, the connection of the top triangles would break, resulting in the loss of isolation.

At stage four (t = 7 min), the {111} planes on the outside sidewalls became the principal etching planes, which merged to form upright pyramid structures (Figure 4g). As expected, the {111} planes of both upright and inverted pyramids were further etched, resulting in valley-shaped openings along the diagonals. While the etching process of the inside {100} plane was terminated, the outside {111} planes continued, resulting in greater depths of the inverted pyramids. On the basis of the morphological transition of the etched nanostructures, we expect that the openings along the diagonals would grow larger as the etching time increased. Finally, the single Si complex nanostructure would break into four smaller nanopyramids with identical shapes and sizes. As a result, the isolated space inside the inverted pyramid no longer existed.

As shown in the top-view SEM images (Figure S3a,b), wafer-scale 3D Si complex structures at stage one (t = 2 min) and stage three (t = 5 min) were fabricated with excellent consistency and uniformity in shape and morphology. After 7 min of KOH etching, the SiO<sub>2</sub> nanoring on the top of the Si complex structure maintained the primary structure as fabricated by DLPL (Figure S4). Most SiO<sub>2</sub> nanorings were

not removed even though the Si undercut was significant. The fabrication of a series of Si 3D nanostructures *via* KOH anisotropic etching demonstrated the potential of DLPL-fabricated SiO<sub>2</sub> nanorings in nanofabrication applications. We expect that DLPL could be used to fabricate more sophisticated patterns and structures.

It has been reported that the light trapping or scattering features of Si nanostructures can enhance the photoelectric performance of perovskite-based devices due to increased light absorption. 60 Therefore, Si complex nanostructures fabricated by 2 min KOH etching were applied to fabricate MAPbI<sub>3</sub>based photodetectors. The fabrication process of the MAPbl<sub>3</sub>based photodetectors is illustrated in Figure 5a. Before the coating process, SiO<sub>2</sub> (~300 nm) was deposited on the Si nanostructures for insulation (Figure 5b). As shown in Figure 5c, the uniform and flat MAPbI<sub>3</sub> film filled the isolated space inside the nanostructures. The side view confirmed that the perovskite film, with a measured thickness of 1330  $\pm$  40 nm, fully covered the Si nanostructures, which had a measured depth of 1290 ± 50 nm. Next, copper (~200 nm) was deposited with a shadow mask to fabricate interdigitated electrodes (Figure S5). The photoresponse of the MAPbI<sub>3</sub>based photodetectors was investigated with illumination from a Xe lamp  $(10 \text{ mW/cm}^2)$ , for which the on/off was manually controlled (experimental details are provided in the Materials and Methods section). The periodic pattern, flat curve at top and bottom, and sharp transition times for each on/off illumination cycle from the photoresponse graph (Figure 5d) demonstrated the high stability and reproducibility of the devices. On the basis of photocurrent measurements, the device also showed 2.5 orders of magnitude increase in the photocurrent ( $\sim$ 36  $\mu$ A) compared to the dark current ( $\sim$ 75 nA), indicating the reliable performance of the fabricated photodetectors. In addition, a MAPbI3 thin film was coated on the Si complex nanostructures fabricated with 7 min KOH etching (Figure S6). Due to the longer anisotropic etching of {100} planes, the thickness of the MAPbI<sub>3</sub> thin film was smaller than the depth of the Si nanostructures. Since the inside space was no longer isolated, the MAPbI<sub>3</sub> thin film was connected on both sides. According to the reported improvement of photocurrent performance with the light-trapping structures, photodetectors fabricated with these types of nanostructures should exhibit improved performance.

### **CONCLUSIONS AND PROSPECTS**

Our results demonstrate that DLPL is a convenient and straightforward method for nanoscale patterning with high throughput and adjustable parameters. The DLPL strategy provides a versatile and practical extension of photolithography to achieve submicron patterning at low cost with high reproducibility. This technique can be integrated into nanoscale device manufacturing for optoelectronics, nanoplasmonics, and biotechnologies, with functions that require 3D nanostructures. Furthermore, with upcoming more systematic and throughout elaborations of DLPL, the resolution could be further improved with different photoresist pairs, resulting in greater capabilities in nanoscale patterning and fabrication. Note that 300 nm is not the lower limit of DLPL; with more precise control of the lithography parameters (exposure, development, photoresist), we anticipate that much smaller features can be realized. Not limited to conventional UV photolithography, this strategy can also be incorporated into other lithographic approaches including DUV, EUV, and EBL to further enhance their resolution.

### **MATERIALS AND METHODS**

**Materials.** Positive photoresist BCI 3511 was purchased from Suzhou Research Materials Microtech Co., Ltd. Negative photoresist 9i was purchased from Suntific Materials (Weifang, China), Ltd. Methylammonium lead iodide (MAPbI $_3$ ) was purchased from Xi'an Polymer Light Technology Corp. Anhydrous potassium hydroxide (KOH) and dimethyl sulfoxide (DMSO) were purchased from Sinopharm Chemical Reagent Co., Ltd. γ-Butyrolactone (GBL) was purchased from Shanghai Aladdin Biochemical Technology Co., Ltd. Magnetron sputtering material SiO $_2$  (99.99%) and evaporation materials, including chromium (99.99%), silver (99.99%), and copper (99.99%), were purchased from ZhongNuo Advanced Material (Beijing, China) Technology Co., Ltd.

**Characterization.** The morphologies of the dual-layer photolithography (DLPL)-fabricated nanorings, KOH-etched 3D Si structures, and surface-coated MAPbI<sub>3</sub> thin film were measured by scanning electron microscopy (SEM, JEOL JSM-6060LA). The photoresponsivity of the MAPbI<sub>3</sub>-based photodetectors was measured using a source meter (Keithley 2602B) on a probe-station.

Fabrication of SiO<sub>2</sub> Nanorings. The SiO<sub>2</sub> nanorings were fabricated with DLPL. First, positive photoresist BCI 3511 was spin-coated on Si substrates at 2500 rpm followed by a 40 s soft bake. Second, negative photoresist 9i was spin-coated on the positive photoresist layer at 4000 rpm followed by a 60 s soft bake. With a mercury—xenon lamp (3500 mW/cm², 365 nm, Hamamatsu Corporation, JP), the dual-layer photoresists were exposed a single time for 30 s, followed by 45 s postbaking. The dual-layer photoresists were developed for 10 and 5 s in a top-down manner, and hollow nanorings were generated. Next, a SiO<sub>2</sub> film was deposited on the substrates via a DM300 magnetron sputtering System (Hefei Jusheng Vacuum Technology Inc.) at 1 nm/min. The remaining photoresists were removed by mild sonication in acetone, while the SiO<sub>2</sub> film on top of the photoresist was lifted off. As a result, SiO<sub>2</sub> nanorings were fabricated on the Si substrate.

Fabrication of Chromium (Cr) or Silver (Ag) Nanorings. The fabrication procedure followed the same fabrication scheme as SiO<sub>2</sub> nanorings by dual-layer photolithography except the SiO<sub>2</sub> deposition

was changed to metal deposition via a DM500 thermal evaporator (Hefei Jusheng Vacuum Technology Inc.). Both Cr and Ag films were deposited at a rate of  $\sim 0.5$  Å/s.

Fabrication of Complex Si Nanostructures. The complex Si nanostructures were fabricated by anisotropic etching with SiO<sub>2</sub> nanorings as the etching mask and 30 wt % KOH solution as the etchant. The substrate was etched at 70 °C with moderate stirring to remove the bubbles on the surface. The addition of isopropyl alcohol mediates the surface roughness of Si in wet etching. The morphology changes of the complex Si nanostructures were monitored *via* scanning electron microscopy (Figure 4d–g) and divided into four etching stages: 2, 3, 5, and 7 min.

Fabrication of MAPbl<sub>3</sub>-Based Photodetectors. The substrates with desired Si complex nanostructures were deposited with ~300 nm SiO<sub>2</sub> at a rate of 1 Å/s *via* thermal evaporation. The perovskite precursor solution (1 M) was prepared by dissolving MAPbl<sub>3</sub> powder in a mixture of GBL and DMSO with a ratio of 7:3 and stirred for 2 h at 60 °C to ensure that the perovskite powder was fully dissolved. The mixture was filtered to remove any insoluble impurities. Then, 50  $\mu$ L of the precursor solution was spin-coated on the SiO<sub>2</sub>/Si substrate with a spin speed of 2500 rpm in the glovebox under an Ar flow. The substrate was annealed at 100 °C for 10 min to form the MAPbl<sub>3</sub> film. Finally, the copper film was deposited on the MAPbl<sub>3</sub> film at a rate of 0.5 Å/s with a shadow mask to fabricate the copper electrode.

### **ASSOCIATED CONTENT**

# Supporting Information

The Supporting Information is available free of charge at https://pubs.acs.org/doi/10.1021/acsnano.1c03703.

Figures of SEM images and table of data of Figure 2c (PDF)

# **AUTHOR INFORMATION**

# **Corresponding Authors**

Xiaobin Xu — Key Laboratory of Advanced Civil Engineering Materials of Ministry of Education, Key Laboratory of D&A for Metal-Functional Materials, School of Materials Science & Engineering, & Institute for Advanced Study, Tongji University, Shanghai 201804, China; ⊚ orcid.org/0000-0002-3479-0130; Email: xiaobinxu@tongji.edu.cn

Paul S. Weiss — California NanoSystems Institute and Department of Chemistry and Biochemistry, University of California, Los Angeles, Los Angeles, California 90095, United States; Department of Bioengineering and Department of Materials Science and Engineering, University of California, Los Angeles, Los Angeles, California 90095, United States; Orcid.org/0000-0001-5527-6248; Email: psw@cnsi.ucla.edu

# Authors

Wenfei Liu – California NanoSystems Institute and Department of Chemistry and Biochemistry, University of California, Los Angeles, Los Angeles, California 90095, United States; orcid.org/0000-0003-1338-7905

Jiabao Wang — Key Laboratory of Advanced Civil Engineering Materials of Ministry of Education, Key Laboratory of D&A for Metal-Functional Materials, School of Materials Science & Engineering, & Institute for Advanced Study, Tongji University, Shanghai 201804, China

Xiuzhen Xu — Key Laboratory of Advanced Civil Engineering Materials of Ministry of Education, Key Laboratory of D&A for Metal-Functional Materials, School of Materials Science & Engineering, & Institute for Advanced Study, Tongji University, Shanghai 201804, China Chuanzhen Zhao — Department of Chemical Engineering, Stanford University, Stanford, California 94305, United States; © orcid.org/0000-0003-0162-1231

Complete contact information is available at: https://pubs.acs.org/10.1021/acsnano.1c03703

## **Author Contributions**

The experiments were designed by W.L., Xiaobin X., and P.S.W. Data were collected by W.L., J.W., Xiuzhen X., and Xiaobin X. and were analyzed by all authors. All the authors contributed to the manuscript writing.

#### Notes

The authors declare no competing financial interest.

### **ACKNOWLEDGMENTS**

This work was financially support by the National Natural Science Foundation of China (Grant No. 51901159) and the Fundamental Research Funds for the Central Universities and the China Postdoctoral Science Foundation (Grant No. 2020M671211). The authors would like to thank Naihao Chiang, Minghe Fang, Hanyue Kang, Zhenkai Ji, and Yuting Xiong for their helpful discussions.

### **REFERENCES**

- (1) Carlson, A.; Bowen, A. M.; Huang, Y.; Nuzzo, R. G.; Rogers, J. A. Transfer Printing Techniques for Materials Assembly and Micro/Nanodevice Fabrication. *Adv. Mater.* **2012**, *24*, 5284–5318.
- (2) Tsai, H.; Pitera, J. W.; Miyazoe, H.; Bangsaruntip, S.; Engelmann, S. U.; Liu, C.-C.; Cheng, J. Y.; Bucchignano, J. J.; Klaus, D. P.; Joseph, E. A.; Sanders, D. P.; Colburn, M. E.; Guillorn, M. A. Two-Dimensional Pattern Formation Using Graphoepitaxy of PS-b-PMMA Block Copolymers for Advanced FinFET Device and Circuit Fabrication. ACS Nano 2014, 8, 5227–5232.
- (3) Shen, B.; Linko, V.; Tapio, K.; Pikker, S.; Lemma, T.; Gopinath, A.; Gothelf, K. V.; Kostiainen, M. A.; Toppari, J. J. Plasmonic Nanostructures through DNA-Assisted Lithography. *Sci. Adv.* **2018**, *4*, eaap8978.
- (4) Wang, C.; Linghu, C.; Nie, S.; Li, C.; Lei, Q.; Tao, X.; Zeng, Y.; Du, Y.; Zhang, S.; Yu, K.; Jin, H.; Chen, W.; Song, J. Programmable and Scalable Transfer Printing with High Reliability and Efficiency for Flexible Inorganic Electronics. *Sci. Adv.* **2020**, *6*, eabb2393.
- (5) Zhao, C.; Liu, Q.; Cheung, K. M.; Liu, W.; Yang, Q.; Xu, X.; Man, T.; Weiss, P. S.; Zhou, C.; Andrews, A. M. Narrower Nanoribbon Biosensors Fabricated by Chemical Lift-Off Lithography Show Higher Sensitivity. *ACS Nano* **2021**, *15*, 904–915.
- (6) Park, S. I.; Xiong, Y.; Kim, R. H.; Elvikis, P.; Meitl, M.; Kim, D. H.; Wu, J.; Yoon, J.; Yu, C. J.; Liu, Z.; Huang, Y.; Hwang, K. c.; Ferreira, P.; Li, X.; Choquette, K.; Rogers, J. A. Printed Assemblies of Inorganic Light-Emitting Diodes for Deformable and Semitransparent Displays. *Science* **2009**, 325, 977–981.
- (7) Choi, C.; Choi, M. K.; Liu, S.; Kim, M. S.; Park, O. K.; Im, C.; Kim, J.; Qin, X.; Lee, G. J.; Cho, K. W.; Kim, M.; Joh, E.; Lee, J.; Son, D.; Kwon, S.-H.; Jeon, N. L.; Song, Y. M.; Lu, N.; Kim, D.-H. Human Eye-Inspired Soft Optoelectronic Device Using High-Density MoS<sub>2</sub>-Graphene Curved Image Sensor Array. *Nat. Commun.* **2017**, *8*, 1664.
- (8) Lin, C.-H.; Cheng, B.; Li, T.-Y.; Retamal, J. R. D.; Wei, T.-C.; Fu, H.-C.; Fang, X.; He, J.-H. Orthogonal Lithography for Halide Perovskite Optoelectronic Nanodevices. *ACS Nano* **2018**, *13*, 1168–1176.
- (9) Lei, Y.; Chen, Y.; Zhang, R.; Li, Y.; Yan, Q.; Lee, S.; Yu, Y.; Tsai, H.; Choi, W.; Wang, K.; Luo, Y.; Gu, Y.; Zheng, X.; Wang, C.; Wang, C.; Hu, H.; Li, Y.; Qi, B.; Lin, M.; Zhang, Z.; et al. A Fabrication Process for Flexible Single-Crystal Perovskite Devices. *Nature* **2020**, 583, 790–795.
- (10) Tang, Q.; Li, H.; Liu, Y.; Hu, W. High-Performance Air-Stable *n*-Type Transistors with an Asymmetrical Device Configuration Based

- on Organic Single-Crystalline Submicrometer/Nanometer Ribbons. J. Am. Chem. Soc. 2006, 128, 14634–14639.
- (11) Zhang, X.; Jie, J.; Deng, W.; Shang, Q.; Wang, J.; Wang, H.; Chen, X.; Zhang, X. Alignment and Patterning of Ordered Small-Molecule Organic Semiconductor Micro-/Nanocrystals for Device Applications. *Adv. Mater.* **2016**, *28*, 2475–2503.
- (12) Moolman, M.; Huang, Z.; Krishnan, S.; Kerssemakers, J. W. J.; Dekker, N. H. Electron Beam Fabrication of a Microfluidic Device for Studying Submicron-Scale Bacteria. *J. Nanobiotechnol.* **2013**, *11*, 12.
- (13) Wang, J.; Li, W.; Zhang, L.; Ban, L.; Chen, P.; Du, W.; Feng, X.; Liu, B.-F. Chemically Edited Exosomes with Dual Ligand Purified by Microfluidic Device for Active Targeted Drug Delivery to Tumor Cells. ACS Appl. Mater. Interfaces 2017, 9, 27441–27452.
- (14) Nouri-Goushki, M.; Sharma, A.; Sasso, L.; Zhang, S.; Van der Eerden, B. C. J.; Staufer, U.; Fratila-Apachitei, L. E.; Zadpoor, A. A. Submicron Patterns-on-a-Chip: Fabrication of a Microfluidic Device Incorporating 3D Printed Surface Ornaments. *ACS Biomater. Sci. Eng.* **2019**, *5*, 6127–6136.
- (15) Dong, P.; Chen, Y.-K.; Duan, G.-H.; Neilson, D. T. Silicon Photonic Devices and Integrated Circuits. *Nanophotonics* **2014**, 3, 215–228.
- (16) Alias, M. S.; Yang, Y.; Ng, T. K.; Dursun, I.; Shi, D.; Saidaminov, M. I.; Priante, D.; Bakr, O. M.; Ooi, B. S. Enhanced Etching, Surface Damage Recovery, and Submicron Patterning of Hybrid Perovskites Using a Chemically Gas-Assisted Focused-Ion Beam for Subwavelength Grating Photonic Applications. *J. Phys. Chem. Lett.* **2016**, *7*, 137–142.
- (17) Higashida, R.; Funabashi, N.; Aoshima, K.-i.; Machida, K. Submicron-Scale Light Modulation Device Driven by Current-Induced Domain Wall Motion for Electro-Holography. *Jpn. J. Appl. Phys.* **2020**, *59*, 053001.
- (18) Wagner, C.; Harned, N. Lithography Gets Extreme. *Nat. Photonics* **2010**, *4*, 24–26.
- (19) Ashby, P. D.; Olynick, D. L.; Ogletree, D. F.; Naulleau, P. P. Resist Materials for Extreme Ultraviolet Lithography: Toward Low-Cost Single-Digit-Nanometer Patterning. *Adv. Mater.* **2015**, 27, 5813–5819.
- (20) Chen, S.; Svedendahl, M.; Antosiewicz, T. J.; Käll, M. Plasmon-Enhanced Enzyme-Linked Immunosorbent Assay on Large Arrays of Individual Particles Made by Electron Beam Lithography. *ACS Nano* **2013**, *7*, 8824–8832.
- (21) Manfrinato, V. R.; Zhang, L.; Su, D.; Duan, H.; Hobbs, R. G.; Stach, E. A.; Berggren, K. K. Resolution Limits of Electron-Beam Lithography toward the Atomic Scale. *Nano Lett.* **2013**, *13*, 1555–1558.
- (22) Kim, S.; Marelli, B.; Brenckle, M. A.; Mitropoulos, A. N.; Gil, E.-S.; Tsioris, K.; Tao, H.; Kaplan, D. L.; Omenetto, F. G. All-Water-Based Electron-Beam Lithography Using Silk as a Resist. *Nat. Nanotechnol.* **2014**, *9*, 306–310.
- (23) Córdoba, R.; Ibarra, A.; Mailly, D.; De Teresa, J. M. Vertical Growth of Superconducting Crystalline Hollow Nanowires by He<sup>+</sup> Focused Ion Beam Induced Deposition. *Nano Lett.* **2018**, *18*, 1379–1386.
- (24) Porrati, F.; Barth, S.; Sachser, R.; Dobrovolskiy, O. V.; Seybert, A.; Frangakis, A. S.; Huth, M. Crystalline Niobium Carbide Superconducting Nanowires Prepared by Focused Ion Beam Direct Writing. ACS Nano 2019, 13, 6287–6296.
- (25) Winkler, R.; Fowlkes, J. D.; Rack, P. D.; Plank, H. 3D Nanoprinting *via* Focused Electron Beams. *J. Appl. Phys.* **2019**, *125*, 210901.
- (26) Xu, X.; Yang, Q.; Cheung, K. M.; Zhao, C.; Wattanatorn, N.; Belling, J. N.; Abendroth, J. M.; Slaughter, L. S.; Mirkin, C. A.; Andrews, A. M.; Weiss, P. S. Polymer-Pen Chemical Lift-Off Lithography. *Nano Lett.* **2017**, *17*, 3302–3311.
- (27) Chou, S. Y.; Krauss, P. R.; Renstrom, P. J. Imprint Lithography with 25-Nanometer Resolution. *Science* **1996**, 272, 85–87.
- (28) Mårtensson, T.; Carlberg, P.; Borgström, M.; Montelius, L.; Seifert, W.; Samuelson, L. Nanowire Arrays Defined by Nanoimprint Lithography. *Nano Lett.* **2004**, *4*, 699–702.

- (29) Guo, L. J. Nanoimprint Lithography: Methods and Material Requirements. *Adv. Mater.* **2007**, *19*, 495–513.
- (30) Huo, F.; Zheng, Z.; Zheng, G.; Giam, L. R.; Zhang, H.; Mirkin, C. A. Polymer Pen Lithography. *Science* **2008**, 321, 1658–1660.
- (31) Qin, D.; Xia, Y.; Whitesides, G. M. Soft Lithography for Microand Nanoscale Patterning. *Nat. Protoc.* **2010**, *5*, 491–502.
- (32) Liao, W. S.; Cheunkar, S.; Cao, H. H.; Bednar, H. R.; Weiss, P. S.; Andrews, A. M. Subtractive Patterning *via* Chemical Lift-Off Lithography. *Science* **2012**, *337*, 1517–1521.
- (33) Hulteen, J. C.; Treichel, D. A.; Smith, M. T.; Duval, M. L.; Jensen, T. R.; Van Duyne, R. P. Nanosphere Lithography: Size-Tunable Silver Nanoparticle and Surface Cluster Arrays. *J. Phys. Chem. B* 1999, 103, 3854–3863.
- (34) Chen, K.; Rajeeva, B. B.; Wu, Z.; Rukavina, M.; Dao, T. D.; Ishii, S.; Aono, M.; Nagao, T.; Zheng, Y. Moiré Nanosphere Lithography. ACS Nano 2015, 9, 6031–6040.
- (35) Hatzor, A.; Weiss, P. S. Molecular Rulers for Scaling Down Nanostructures. *Science* **2001**, 291, 1019–1020.
- (36) McLellan, J. M.; Geissler, M.; Xia, Y. Edge Spreading Lithography and Its Application to the Fabrication of Mesoscopic Gold and Silver Rings. J. Am. Chem. Soc. 2004, 126, 10830–10831.
- (37) Geissler, M.; McLellan, J. M.; Xia, Y. Edge-Spreading Lithography: Use of Patterned Photoresist Structures to Direct the Spreading of Alkanethiols on Gold. *Nano Lett.* **2005**, *5*, 31–36.
- (38) Halpern, A. R.; Corn, R. M. Lithographically Patterned Electrodeposition of Gold, Silver, and Nickel Nanoring Arrays with Widely Tunable Near-Infrared Plasmonic Resonances. *ACS Nano* **2013**, *7*, 1755–1762.
- (39) Xu, X.; Yang, Q.; Wattanatorn, N.; Zhao, C.; Chiang, N.; Jonas, S. J.; Weiss, P. S. Multiple-Patterning Nanosphere Lithography for Fabricating Periodic Three-Dimensional Hierarchical Nanostructures. *ACS Nano* **2017**, *11*, 10384–10391.
- (40) Switkes, M.; Rothschild, M. Immersion Lithography at 157 nm. *J. Vac. Sci. Technol., B: Microelectron. Process. Phenom.* **2001**, *19*, 2353–2356.
- (41) Ghaida, R. S.; Torres, G.; Gupta, P. Single-Mask Double-Patterning Lithography for Reduced Cost and Improved Overlay Control. *IEEE Trans. Semicond. Manuf.* **2011**, 24, 93–103.
- (42) Liu, S.; Al-Shadeedi, A.; Kaphle, V.; Keum, C.-M.; Lüssem, B. Patterning Organic Transistors by Dry-Etching: The Double Layer Lithography. *Org. Electron.* **2017**, *45*, 124–130.
- (43) Huo, F.; Zheng, G.; Liao, X.; Giam, L. R.; Chai, J.; Chen, X.; Shim, W.; Mirkin, C. A. Beam Pen Lithography. *Nat. Nanotechnol.* **2010**, *5*, 637–640.
- (44) Feng, B. C.; Feng, G. C. Two Layer Resist System. U.S. Patent 4,204,009, 1980.
- (45) Lau, J. W.; Shaw, J. M. Magnetic Nanostructures for Advanced Technologies: Fabrication, Metrology and Challenges. *J. Phys. D: Appl. Phys.* **2011**, *44*, 303001.
- (46) Preiss, E. M.; Krauss, A.; Seidel, H. Sputtered Pt Electrode Structures with Smoothly Tapered Edges by Bi-Layer Resist Lift-Off. *Thin Solid Films* **2015**, *597*, 158–164.
- (47) Chiriacò, M. S.; Bianco, M.; Amato, F.; Primiceri, E.; Ferrara, F.; Arima, V.; Maruccio, G. Fabrication of Interconnected Multilevel Channels in a Monolithic SU-8 Structure Using a LOR Sacrificial Layer. *Microelectron. Eng.* **2016**, *164*, 30–35.
- (48) Bean, K. E. Anisotropic Etching of Silicon. *IEEE Trans. Electron Devices* 1978, 25, 1185–1193.
- (49) Yamada, K.; Yamada, M.; Maki, H.; Itoh, K. M. Fabrication of Arrays of Tapered Silicon Micro-/Nano-Pillars by Metal-Assisted Chemical Etching and Anisotropic Wet Etching. *Nanotechnology* **2018**, *29*, 28LT01.
- (50) Xu, X.; Liu, W.; Ji, Z.; Hao, D.; Yan, W.; Ye, Z.; Hu, Y.; Fang, M.; Wang, C.; Ma, L.; Huang, J.; Xu, X.; Weiss, P. S. Large-Area Periodic Organic-Inorganic Hybrid Perovskite Nanopyramid Arrays for High Performance Photodetector and Image Sensor Applications, in preparation, 2021.
- (51) Deng, W.; Lv, Y.; Zhang, X.; Fang, X.; Lu, B.; Lu, Z.; Jie, J. High-Resolution Patterning of Organic Semiconductor Single Crystal

- Arrays for High-Integration Organic Field-Effect Transistors. *Mater. Today* **2020**, *40*, 82–90.
- (52) Deng, W.; Jie, J.; Xu, X.; Xiao, Y.; Lu, B.; Zhang, X.; Zhang, X. A Microchannel-Confined Crystallization Strategy Enables Blade Coating of Perovskite Single Crystal Arrays for Device Integration. *Adv. Mater.* **2020**, *32*, 1908340.
- (53) Hines, D. R.; Siwak, N. P.; Mosher, L. A.; Ghodssi, R. MEMS Lithography and Micromachining Techniques. In *MEMS Materials and Processes Handbook*; Ghodssi, R., Lin, P., Eds.; Springer Nature, 2011; pp 667–753.
- (54) Morton, K. J.; Nieberg, G.; Bai, S.; Chou, S. Y. Wafer-Scale Patterning of Sub-40 nm Diameter and High Aspect Ratio (>50:1) Silicon Pillar Arrays by Nanoimprint and Etching. *Nanotechnology* **2008**, *19*, 345301.
- (55) Garnett, E.; Yang, P. Light Trapping in Silicon Nanowire Solar Cells. *Nano Lett.* **2010**, *10*, 1082–1087.
- (56) Ge, M.; Rong, J.; Fang, X.; Zhou, C. Porous Doped Silicon Nanowires for Lithium Ion Battery Anode with Long Cycle Life. *Nano Lett.* **2012**, *12*, 2318–2323.
- (57) Huo, C.; Wang, J.; Fu, H.; Li, X.; Yang, Y.; Wang, H.; Mateen, A.; Farid, G.; Peng, K. Q. Metal-Assisted Chemical Etching of Silicon in Oxidizing HF Solutions: Origin, Mechanism, Development, and Black Silicon Solar Cell Application. *Adv. Funct. Mater.* **2020**, *30*, 2005744.
- (58) Seidel, H.; Csepregi, L.; Heuberger, A.; Baumgärtel, H. Anisotropic Etching of Crystalline Silicon in Alkaline Solutions: I. Orientation Dependence and Behavior of Passivation Layers. *J. Electrochem. Soc.* **1990**, *137*, 3612–3626.
- (59) Mavrokefalos, A.; Han, S. E.; Yerci, S.; Branham, M. S.; Chen, G. Efficient Light Trapping in Inverted Nanopyramid Thin Crystalline Silicon Membranes for Solar Cell Applications. *Nano Lett.* **2012**, *12*, 2792–2796.
- (60) Mao, J.; Sha, W. E. I.; Zhang, H.; Ren, X.; Zhuang, J.; Roy, V. A. L.; Wong, K. S.; Choy, W. C. H. Novel Direct Nanopatterning Approach to Fabricate Periodically Nanostructured Perovskite for Optoelectronic Applications. *Adv. Funct. Mater.* **2017**, *27*, 1606525.